ROYAL SOCIETY
OF CHEMISTRY

PAPER

Check for updates

Metal oxide patterns of one-dimensional nanofibers: on-demand, direct-write fabrication, and application as a novel platform for gas detection†

Kyeorei Lim,[a] Young-Moo Jo,[a] Ji-Wook Yoon [ID] *[b] and Jong-Heun Lee [ID] *[a]

To organize one-dimensional (1D) metal oxides into highly ordered and controllable architectures on the required regions remains challenging. Herein, we report for the first time the facile, versatile, and on-demand fabrication of metal oxide patterns comprising 1D nanofibers *via* near-field electrospinning (NFES), which have a wide variety of potential applications in sensors, optoelectronic circuits, and functional nanoelectronics. Grids, diamonds, and hexagrams of In_2O_3, Co_3O_4, and NiO nanofibers are first demonstrated, and the underlying mechanisms for fiber formation are systematically investigated with respect to the experimental parameters of NFES. Furthermore, we propose the nano-architectures as a novel gas sensing platform that exhibits an unprecedentedly high gas response (resistance ratio, S_T = 239, T: trimethylamine) and selectivity ($S_T S_E^{-1}$ > 7, E: ethanol) to 5 ppm trimethylamine compared with thin film counterparts (S_T = 24, $S_T S_E^{-1} \approx 1$). The research provides a vital breakthrough to fabricate metal oxide nano-architectures of 1D nanofibers and new platforms to design next-generation functional nanodevices for a wide range of emerging applications.

Introduction

One-dimensional (1D) nanostructures have drawn considerable attention as functional nano-building blocks for scientific studies and technological applications. One of the most important challenges in this area is to organize 1D nanostructures into highly ordered and controllable architectures on the required regions. For this, near-field electrospinning (NFES) capable of the direct writing of 1D nanofibers on substrates has been proposed,[1] which has advantages such as simple, cost-effective, and high-throughput processing over serial patterning methods including e-beam writing,[2,3] photolithography,[4,5] and nanomolding.[6–8] The basic principle is similar to that of conventional electrospinning (c-ES), in which a whipping polymer jet elongated from a metallic nozzle by an electric voltage (10–30 kV) is randomly deposited on a counter collector placed 10–30 cm away from the nozzle.[9] However, NFES has three distinctive features: (1) the low applied voltage (<1 kV), (2) the short distance between the nozzle and the collector (<a few mm), and (3) the use of a moving nozzle and/or collector, which facilitates position-tunable aligning and on-demand patterning of 1D polymer fibers on the substrates.

To date, various metal oxide nanofibers have been prepared *via* c-ES of polymeric fibers containing metal salts and subsequent heat treatment.[10–13] Nevertheless, the fabrication of well-organized patterns of 1D metal oxide nanofibers using NFES has been barely reported, although elaborate architectures of polymer fibers have been demonstrated over a decade ago.[1,14] This suggests that it is still challenging to form the straight configuration of metal oxide nanofibers *via* NFES. The key reason is the difficulty of the fabrication of 1D precursor fibers due to the chaotic whipping motion of the jet caused by the acceleration of metal ions under the electric field.[15] Although highly non-polar solvents (*e.g.*, tetrahydrofuran) or metal alkoxides with a relatively low dependence on the electric field have been investigated,[16,17] the toxicity and high cost of the chemicals restrict the widespread use of NFES for the synthesis of diverse metal oxide nanofibers. Therefore, it is of crucial importance to develop a new and general strategy to prepare well-designed metal oxide nanofibers *via* NFES using easily available inorganic salts (*e.g.*, nitrates) and less-toxic solvents. Moreover, to the knowledge of the authors, the facile and versatile fabrication of metal oxide nano-architectures comprising 1D nanofibers has never been demonstrated thus far.

Herein, we report for the first time the on-demand, direct-write fabrication of metal oxide nano-architectures *via* NFES. In_2O_3, Co_3O_4, and NiO nanofiber arrays and patterns were

[a]*Department of Materials Science and Engineering, Korea University, Seoul 02841, Republic of Korea. E-mail: jongheun@korea.ac.kr*

[b]*Department of Information Materials Engineering, Division of Advanced Materials, Jeonbuk National University, Jeonju 54896, Republic of Korea. E-mail: jwyoon@jbnu.ac.kr*

This journal is © The Royal Society of Chemistry 2019

J. Mater. Chem. A, 2019, **7**, 24919–24928 | 24919

fabricated *via* NFES of precursor solutions prepared by dissolving metal nitrates and polyvinylpyrrolidone (PVP) in less-toxic methanol, followed by heat treatment at 600 °C for 5 h. The formation mechanisms of the precursor fibers and metal oxide nano-architectures were investigated in relation to the precursor solution parameters, such as the volatility, electrical conductivity, and viscosity, as well as the working parameters, including the needle-to-collector distance and the moving velocity of the nozzle and collector. Moreover, we propose the nano-architectures as a novel gas sensing platform that exhibits unprecedentedly high selectivity and response to trimethylamine compared with other metal oxide nanostructures (*e.g.*, nanofiber mats) reported in the literature. The novel metal oxide nano-architectures allow the development of a new class of high-performance nanodevices, including sensors, optoelectronic circuits, biomimetic systems, and functional electronics.

Experimental

Fabrication of In_2O_3, Co_3O_4, and NiO nanofiber patterns and sensors

Polyvinylpyrrolidone (PVP, 17.4 wt%, M_w = 1 300 000, Sigma-Aldrich Co., Ltd., USA) and metal nitrates (indium nitrate hydrate, 1.4 wt%, 99.999%; cobalt nitrate hexahydrate, 1.7 wt%, 99.99%; nickel nitrate hexahydrate, 1.7 wt%, 99.99%; Sigma-Aldrich Co., Ltd., USA) were dissolved into 7 g of methanol (99%, Samchun Chemical Co., Ltd., Republic of Korea), and kept under magnetic stirring (500 rpm) for 24 h at room temperature. The prepared homogeneous solution was transferred to a glass syringe (1000 μL) equipped in a syringe loader with a 21-gauge needle, and electrospun onto a 4-inch Si/SiO$_2$ wafer above a metallic collector, with a flow rate of 0.005 μL min^{-1} at an applied voltage of 50 V over a needle-to-collector distance of 1 mm. During electrospinning, the loader and collector moved toward *x*- and/or *y*-axis at a controlled moving velocity of 800 mm s^{-1}, leading to the fabrication of precursor fiber patterns, for example, grids, diamonds, and hexagrams. The precursor patterns were annealed at 600 °C for 5 h in an air atmosphere, and converted into the corresponding patterns of In_2O_3, Co_3O_4, and NiO nanofibers, respectively. For gas sensor application, grid patterns (grid width of 200 μm) of In_2O_3, Co_3O_4, and NiO nanofibers were formed on the 4-inch Si/SiO$_2$ wafer containing 76 sensor substrates (size: 1 × 1 cm^2) in which Pt interdigitated electrodes are on the top surface (electrode width: 50 μm, electrode spacing: 5 μm).

Fabrication of In_2O_3, Co_3O_4, and NiO thin film sensors

In_2O_3, Co_3O_4, and NiO thin film sensors were prepared by electron-beam evaporation (Rocky Mountain Vacuum Tech. Inc., USA) at 25 °C on the sensor substrate. The base pressure was maintained in the range of 10^{-6} torr. The voltage and the current of the electron-beam were set at 7.1 kV and 50 mA, respectively, which led to a deposition rate of 0.1 Å s^{-1}. The as-prepared In_2O_3, Co_3O_4, and NiO thin films were annealed at 600 °C for 5 h at an air atmosphere to promote crystallization and oxidation of In_2O_3, Co_3O_4, and NiO thin films.

Fabrication of In_2O_3 nanofiber mats sensors

12.5 wt% of PVP (M_w = 1 300 000, Sigma-Aldrich Co., Ltd., USA), and 4 wt% of indium nitrate hydrate (99.999%, Sigma-Aldrich Co., Ltd., USA) were dissolved in 10 g of *N,N*-dimethylformamide (99.5%, Samchun Pure Chemical Co., Ltd., Republic of Korea) and stirred at 500 rpm for 24 h. The prepared homogeneous solution was loaded in 20 mL of syringe, and electrospun on a metallic collector using a 25-gauge needle with a flow rate of 0.01 mL h^{-1} at an applied voltage of 17 kV over a collection distance of 20 cm. The as-spun nanofibers were dried at 70 °C for 24 h to remove residual solvents, and converted into In_2O_3 nanofibers by heat treatment at 600 °C for 2 h in an air atmosphere. The In_2O_3 nanofibers were mixed with an organic binder (FCM, a terpineol-based ink vehicle, USA) in the ratio of 47 : 53 wt% to form a slurry. The sensing film was coated on the sensor substrate by screen-printing the slurry. The screen-printed sensing layer was heat-treated at 600 °C for 2 h to remove organic contents.

Gas sensing characteristics

The sensors, the Si/SiO$_2$ substrates with Pt electrodes coated with sensing materials, were placed in a quartz tube furnace and heated at sensing temperature (In_2O_3: 350 °C; Co_3O_4: 225 °C; NiO: 300 °C). The atmosphere was controlled using a four-way valve to ensure a constant flow of dry air at the rate of 200 mL min^{-1} and to introduce the analytic gas. The gas concentration was controlled by changing the mixing ratio of the parent gases (5 ppm of TMA, ethanol, ammonia, *p*-xylene, toluene, benzene, ethylene, and CO, all in air balance) and dry synthetic air. The dc-probe resistance of the sensor was measured using an electrometer interfaced with a computer.

Characterization

The morphologies of prepared materials were observed by using digital camera (FMVU-03MTC-CS, Point grey, Canada) and field emission scanning electron microscopy (SEM, SU-70, Hitachi Co., Ltd., Japan). Energy dispersive spectroscopy (EDS) mapping was performed by using SME (SU-70, Hitachi Co., Ltd., Japan). The phase and crystal structure of metal oxide patterns were analyzed by using X-ray diffractometry (XRD, D/MAX-2500, Rigaku Ltd., Japan) with CuKα radiation (λ = 1.5418 Å). The electrical conductivity and viscosity of solutions were measured by conductivity meter (HI8733N, Hanna Instruments, Woonsocket, RI, USA) and viscometer (DV-E viscometer, Brookfield Engineering Laboratories, Inc., USA) at 25 °C, respectively. The weight loss (%) of precursor fibers during heat treatment was investigated by using thermogravimetric analysis (TGA, SDT Q600 V20.9 Build 20, TA Co., Ltd., USA) from 20 to 600 °C with heating rate of 1 °C min^{-1} at air atmosphere.

Results & discussion

The precursor patterns for the metal oxide nano-architectures were prepared using an electrohydrodynamic jet printer

24920 | *J. Mater. Chem. A*, 2019, **7**, 24919–24928

This journal is © The Royal Society of Chemistry 2019

(eNano Printer, Enjet Inc., Korea) (Fig. 1a). The printer comprised two main components: a syringe loader and a metallic collector. The loader had a detachable needle and allowed to adjust the flow rate (Q) of the precursor solutions and the needle-to-collector distance (d_z). The substrates (*e.g.*, 4-inch SiO_2/Si wafer) were attached to the collector by a back pressure provided through the internal pinholes, which prevented the movement of the substrates as the collector moved rapidly (maximum velocity of 800 mm s^{-1}). To perform electrospinning, a glass syringe containing the solution (1000 µL) was mounted onto the loader, and a voltage (0–4 kV) was applied. The loader and collector moved toward the *x*- and *y*-axis, respectively, with a controlled velocity (v). Accordingly, the on-demand and continuous fabrication of polymeric architectures was possible, ranging from a single fiber to elaborate fiber patterns (Fig. 1b–d). The morphology of the fibers was significantly influenced by the experimental parameters, such as the volatility, conductivity, and viscosity of the precursor solution, as well as d_z and v. The metal oxide nanofiber arrays and patterns were prepared *via* heat treatment of the as-spun architectures at 600 °C for 5 h (Fig. 1e). The detailed synthesis conditions are presented in Experimental section.

We demonstrated the direct writing of patterns such as grids, diamonds, and hexagrams on a 4-inch SiO_2/Si wafer (Fig. 2a1–c1). Each pattern was fabricated *via* NFES of precursor solutions containing indium, cobalt, and nickel, respectively. The compositions of the solutions and working parameters (*e.g.*, d_z and v) are presented in Table 1. All the patterns comprised a straight configuration of polymeric composites, and their fibrous (*i.e.*, cylindrical) morphology with a diameter of ∼1 µm was confirmed *via* side-view scanning electron microscopy (SEM) (Fig. S1a1–c1†). The presence of indium, cobalt, and nickel in the fibers was confirmed *via* energy-dispersive X-ray spectroscopy (Fig. S1a2–c2†). After heat treatment at 600 °C for 5 h, the patterns of the precursor fibers were converted into the corresponding metal oxide nano-architectures (Fig. 2a2–c2). The fiber diameters decreased to <200 nm, while the cylindrical morphology was maintained (Fig. 2a3–c3). X-ray diffraction (XRD) analysis (Fig. 2a4–c4) confirmed the crystallinity and phase of In_2O_3, Co_3O_4, and NiO.

To fabricate and optimize the nano-architectures, we investigated various precursor solutions, which were prepared by altering the solvent and the concentration of PVP and metal salts (Table S1†). Note that the volatility, viscosity, and conductivity of the precursor solutions were the representative solution parameters of c-ES. In this study, the effect of the solvent volatility was examined first, as it is a primary factor to the electrospinnability of precursor solutions.[18] For this, three different solutions were prepared by dissolving the same amounts of indium nitrate (0.125 g, 1.4 wt%) and PVP (1.5 g, 17.4 wt%) in 7 g of water, ethanol, or methanol, which were electrospun into In/PVP fiber arrays at identical V (50 V), Q (0.005 µL min^{-1}), d_z (1 mm), and v (800 mm s^{-1}). For simplicity, the fibers synthesized using the water, ethanol, and methanol solvents are referred to as W-, E-, and M-fibers, respectively.

A stable conical electrostatic jet (*i.e.*, Taylor cone) in each solution was well-established at 50 V (Fig. 3a1–c1), leading to the direct-write fabrication of periodic arrays on the substrate (array spacing of 100 µm) (Fig. 3a2–c2). However, the W-fibers were significantly thicker than the others (Fig. 3a3–c3). The side SEM observations (insets of Fig. 3a3–c3) revealed that the W-fibers did not have a circular cross section and were nearly wetted on the substrate (contact angle ≈ 0°). In c-ES, such wetting occurs when a viscous fluid jet extracted from the Taylor cone is not fully dried while being stretched toward the collector by an electric field.[19,20] Thus, the wetting of the W-fibers was due to incomplete evaporation of the water solvent during the NFES. The E-fibers exhibited a partial wetting configuration with an increased contact angle (∼30°), whereas the M-fibers exhibited a perfect cylindrical morphology with negligible wetting. These results strongly suggest that the wetting phenomenon was closely related to the volatility of the solvents. The d_z value (1 mm) in the present study was significantly lower than those for c-ES (10–30 cm). Thus, the distance could be too short for the water and ethanol which are less volatile than methanol to evaporate completely before deposition. Note that the boiling points of the solvents decreased in the following order: water (100 °C) > ethanol (78.4 °C) > methanol (64.7 °C). To achieve cylindrical fibers regardless of the solvent, the drying of most of the solvent before writing *via* the increase of d_z may be
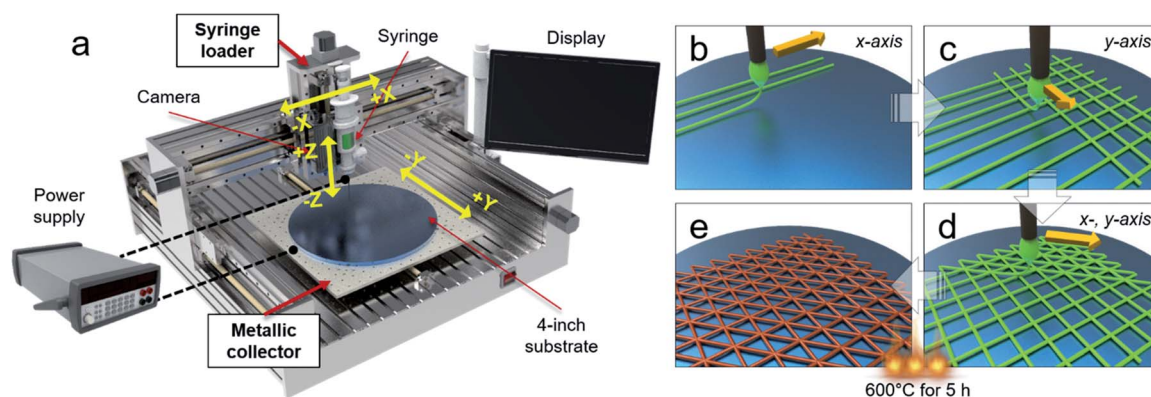

Fig. 1 (a) Schematic of the electrohydrodynamic jet printer for NFES. (b–e) Fabrication procedure for a pattern composed of 1D metal oxide nanofibers.

This journal is © The Royal Society of Chemistry 2019

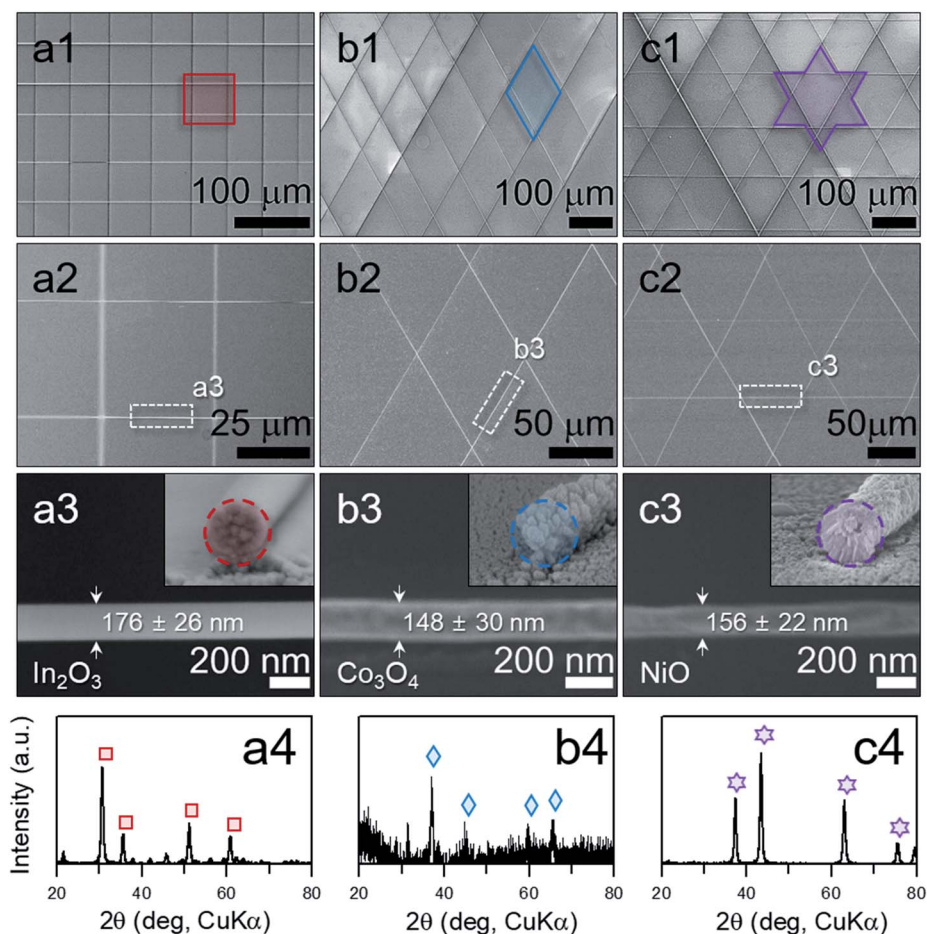*J. Mater. Chem. A*, 2019, **7**, 24919–24928 | **24921**

Fig. 2 (a1–c1) SEM images of (a1) In/PVP grids, (b1) Co/PVP diamonds, and (c1) Ni/PVP hexagrams; (a2–c3) corresponding metal oxide patterns consisting of (a2 and a3) In_2O_3, (b2 and b3) Co_3O_4, and (c2 and c3) NiO nanofibers (number of measurement for determining the width of nanofiber: 10). (a4–c4) XRD patterns of (a4) In_2O_3 grids, (b4) Co_3O_4 diamonds, and (c4) NiO hexagrams.

considered but significantly hinders the precise arraying and patterning of fibers. The reason for this is discussed in the later section.

Distinctly different In_2O_3 structures were formed by annealing the aforementioned precursor fibers at 600 °C for 5 h (Fig. 3a4–c4). Note that heat treatment at ≥600 °C was essential to remove the PVP completely (Fig. S2†). The In_2O_3 arrays derived from M-fibers exhibited a well-defined fibrous morphology (Fig. 3a4), whereas the specimens prepared by annealing the E- and W-fibers exhibited band-like assemblies of metal-oxide nanoislands (Fig. 3b4 and c4). The formation of discrete islands in the E- and W-fibers is attributed to the

wetting of the polymeric fibers, the decomposition of polymeric components, and the oxidation of metal ions *via* thermal annealing.[21] This suggests that the NFES-fabricated precursor fibers with a non-wetting configuration were advantageous to be converted into continuous metal oxide fibers *via* heat treatment. Thus, it is beneficial to use highly volatile solvents (*e.g.*, methanol) for the preparation of metal oxide nanofibers, as well as their precursor fibers, *via* NFES.

The viscosity (η) of the precursor solution is another key parameter affecting the morphology of fibers in c-ES. At a low viscosity, drops or beads are formed, and excessive viscosity causes clogging at the needle tip. In c-ES, the range of viscosity

Table 1 Solution compositions and experimental parameters for the direct writing of nanofiber patterns

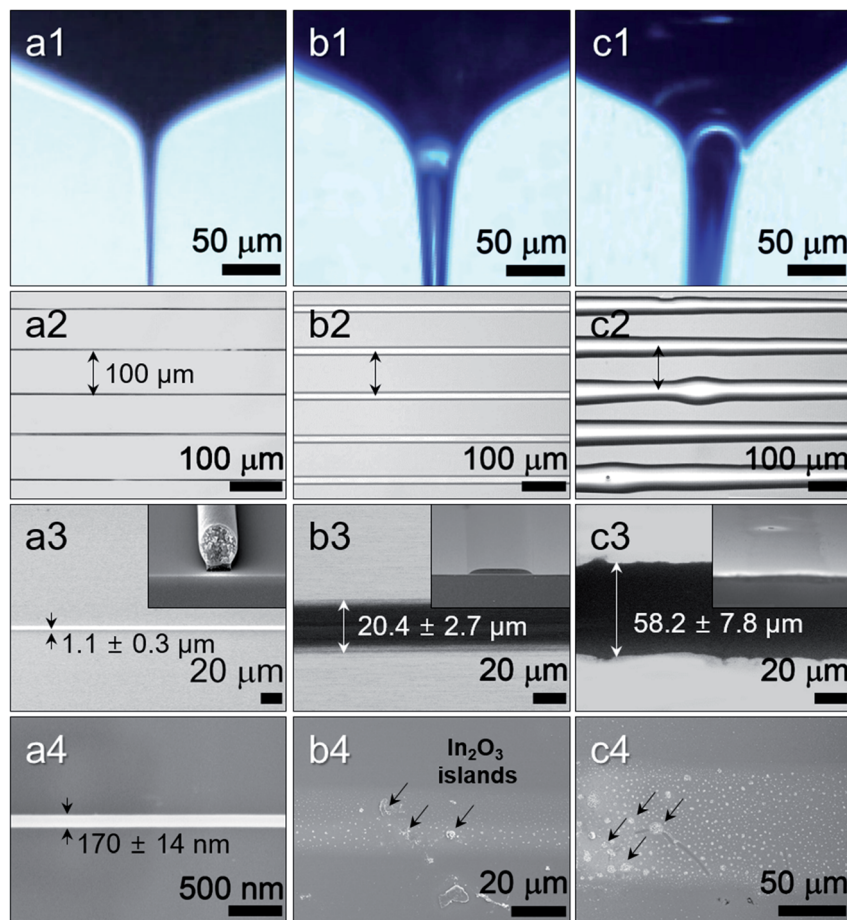| Solvent (g)	Polymer (wt%)	Metal salts (wt%)	Voltage (V)	Q (μL min^{-1})	d_z (mm)	v (mm s^{-1})
Methanol (7)	17.4	Indium (1.4)	50	0.005	1	800
Methanol (7)	17.4	Cobalt (1.7)	50	0.005	1	800
Methanol (7)	17.4	Nickel (1.7)	50	0.005	1	800

Fig. 3 (a1–c1) Optical images of electrostatic jets from the solutions prepared using (a1) methanol, (b1) ethanol, and (c1) water as solvents. (a2–c2) Optical and (a3–c3) SEM images of In/PVP arrays synthesized *via* NFES using the corresponding solutions. (a4–c4) SEM images of In_2O_3 structures prepared *via* heat treatment at 600 °C for 5 h (number of measurement for determining the width of nanofiber: 10).

for ensuring the continuous synthesis of fibers is generally <500 mPa s [22–27] when both metal salts and PVP (molecular weight = 1 300 000) are used (Table S2†). In comparison, in the present study, the optimum viscosity of the solution for M-fibers measured by a viscometer (DV-E, Brookfield, Canada) was more than three times higher (~1500 mPa s). To identify the suitable viscosity range to form fibrous structures *via* NFES, we prepared five solutions with different PVP concentrations (4.7–19.7 wt%) at fixed amounts of indium nitrate (1.4 wt%) and methanol (7 g) and performed NFES. When the PVP concentration was >17.4 wt% (*i.e.*, 19.7 wt%; $\eta > \sim 2500$ mPa s), precursor fibers were not formed, because the tip of the needle was blocked at the beginning stage. In contrast, well-aligned arrays were formed by using solutions with lower concentrations of PVP (≤12.8 wt%; $\eta < \sim 500$ mPa s) (Fig. 4a1 and b1). However, the individual fibers exhibited wetting configurations (insets of Fig. 4a1 and b1) and were transformed into In_2O_3 islands after heat treatment (Fig. 4a2 and b2).

The optimum viscosity for NFES ranged from 500 to 2500 mPa s (Fig. 4c), which is significantly higher than that for c-ES (<500 mPa s). However, from the viewpoint of solvent evaporation, a high viscosity (and thus a high polymer concentration) is

unfavorable to prepare non-wetted fibers, because of the boiling point elevation. This strongly suggests that another mechanism is involved in the formation of fibers in NFES. The fundamental mechanisms for fiber formation in c-ES and NFES are identical except for a few differences in the working conditions (*e.g.*, d_z). When a jet starts to elongate from the Taylor cone owing to electric fields, the polymer concentration increases as the solvent volume fraction decreases rapidly. Consequently, the polymer chains overlap and become entangled (*i.e.*, chain entanglement); thus, the breakup of the jet into droplets is prevented.[28] The viscoelastic jet stretches toward the collector, while the entanglements increase with solvent evaporation, resulting in the formation of solid fibers.

In c-ES, the prerequisite for fiber formation is a bare minimum polymer concentration, which ensures the formation of the viscoelastic jet.[29] This is because the high solvent evaporation at a high d_z facilitates the entanglement; thus, the elongated jet readily turns into a solid fibrous framework during the process. In contrast, in NFES, it is difficult to form fibers with such a dilute solution, as the framework formation is retarded at a short d_z (low solvent evaporation). Hence, a more concentrated solution, in which effective chain entanglements
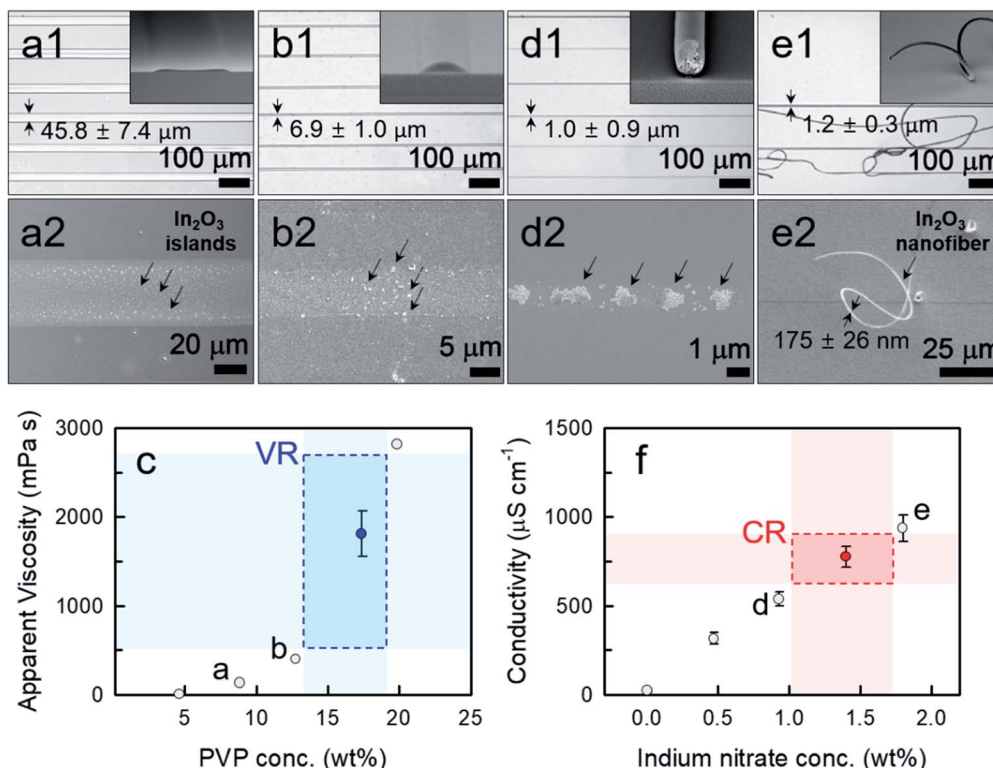
Fig. 4 (a1 and b1) Optical and SEM images of In/PVP arrays prepared using solutions containing (a1) 8.9 wt% or (a2) 12.8 wt% PVP and 1.4 wt% indium nitrate. (a2 and b2) SEM images of In_2O_3 shaped *via* heat treatment of the In/PVP arrays. (c) Solution viscosity with respect to the concentration of PVP (the concentration of indium nitrate was fixed at 1.4 wt%). (d1 and e1) Optical and SEM images of In/PVP arrays prepared using solutions containing (d1) 0.93 wt% or (e1) 1.8 wt% indium nitrate and 17.4 wt% PVP. (d2 and e2) SEM images of In_2O_3 structures prepared *via* heat treatment of the In/PVP arrays. (f) Solution conductivity with respect to the concentration of indium nitrate (the concentration of PVP was fixed at 17.4 wt%). VR: viscosity regime for fiber formation; CR: conductivity regime for fiber formation. The average width of 10 nanofibers was measured for each condition and average apparent viscosity and conductivity of 3 solutions were measured.

can occur, is required if the d_z is not sufficiently long. Note that the polymer jets with a higher viscosity form a solid structure faster than those with a lower viscosity.[30] From this perspective, a high solution viscosity is advantageous for NFES. However, when the viscosity is excessive (above a threshold), the solid framework forms too early, leading to the failure of electrospinning. This explains the optimum window of the solution viscosity (500–2500 mPa s).

The non-wetted fibers were well-developed when the solution viscosity was in the optimum window, regardless of the indium nitrate concentration (which was varied in the range of 0–1.8 wt%). However, the fiber alignments differed depending on the indium nitrate concentration (Fig. 4d1 and e1). For instance, when the indium nitrate content was high (1.8 wt%), the precursor fibers were not aligned but randomly deposited on the substrate (Fig. 4e1). Thus, the heat-treated precursor fibers (*i.e.*, In_2O_3 nanofibers) exhibited a tangled morphology (Fig. 4e2).

Fiber alignment in electrospinning remains challenging owing to the chaotic whipping motion of the jet under electric fields. Although the jet path is nearly straight at an early stage (*i.e.*, stable zone), it becomes chaotic after a distance of 1–3 mm,[1,31] as the mutual repulsion of charges on the jet rapidly increases with the solvent evaporation. Accordingly, randomly

oriented fibers are generally formed at a high d_z (10–30 cm) in c-ES. NFES is capable of producing aligned fibers because the d_z is comparable to the length of the stable zone.[1] However, when the solution contains abundant metal ions, the alignment becomes more difficult even in NFES, because the jet instability increases with the surface charge density,[32] reducing the length of the stable zone. Thus, an excessive solution conductivity (σ) hampers the formation of aligned fibers. The conductivity of the solution with 1.8 wt% indium nitrate was ~1480 μS cm^{-1}. This suggests that the solution conductivity should be lower than ~1480 μS cm^{-1} to prepare aligned fibers *via* NFES. When the solution conductivity was too low (*e.g.*, 0.93 wt%, $\sigma \approx 980$ μS cm^{-1}), well-aligned precursor fibers were produced (Fig. 4d1), but the fibrous structure collapsed into discrete islands after heat treatment (Fig. 4d2). This was possibly due to the lack of sufficient indium sources enough to form a continuous fiber during the heat treatment, indicating that the concentration of indium nitrate should be >0.93 wt%. Therefore, for preparing aligned and continuous In_2O_3 nanofibers using NFES, the indium nitrate concentration needs to be in the range of 0.93–1.8 wt% (Fig. 4f).

In addition to the solution parameters, the working parameters, such as d_z and v, should be considered to design aligned fibers using NFES. Thus, we investigated the effect of d_z at

a fixed v (800 mm s^{-1}). The NFES solution was the same one that was used for the M-fiber synthesis. When d_z was too short ($\leq$0.5 mm) (Fig. S3a†), wetted precursor fibers were formed because of the difficulty of the complete evaporation of the solvent during the electrospinning. When d_z was too high ($\geq$1.5 mm) (Fig. S3b†), whipping occurred; hence, tangled precursor fibers were formed. This indicates that the optimum range of d_z for non-wetted, aligned fibers is 0.5–1.5 mm (*e.g.*, 1 mm). Zheng *et al.*[31] reported that d_z should be in the range of 1–3 mm to prepare aligned fibers *via* NFES. However, they used a solution containing a polymer only (*i.e.*, polyethylene oxide). In the present study, the addition of the metal source significantly increased the solution conductivity; thus, the alignment of the precursor fibers was more disturbed. Therefore, the range of d_z became narrower (0.5–1.5 mm).

The effect of v was examined at a fixed d_z (1 mm). The wetting of fibers was observed at a low v ($\leq$400 mm s^{-1}) (Fig. S4a†). The wetting decreased with an increase in v and finally became negligible at v = 800 mm s^{-1} (Fig. S4b and c†). This indicates that a high v is favorable to promote solvent evaporation, as reported in the literature.[31] Additionally, a high v facilitated the alignment of fibers. The precursor fibers were well-aligned at v = 800 mm s^{-1} (Fig. S4c1†) but exhibited disorder at v $\leq$ 400 mm s^{-1} (Fig. S4a1 and b1†). This is consistent with the explanation that the fiber alignment is hindered at a low v owing to the failure of the repulsive force of the external electric field to offset the oscillation motion of the charged jet.[31] Thus, a high v is needed to prepare well-aligned and non-wetted fibers *via* NFES.

We systematically investigated the effects of the experimental parameters on the fiber formation in NFES and examined the relevant underlying mechanisms. All the parameters had an optimum range, indicating that the sophisticated control or tuning of the parameters is essential to prepare well-organized and continuous precursor and/or metal oxide fibers *via* NFES. The effects of the solution and working parameters on the alignment and wetting/non-wetting behaviors of the precursor fibers and the resulting metal oxide nanostructures are presented in Fig. 5.

As the first application of the patterns, we fabricated gas sensors by producing a large-scale grid pattern of In$_2$O$_3$ nanofibers (grid width of 200 μm) on a 4-inch SiO$_2$/Si wafer consisting of 76 sensor substrates, and evaluated sensing properties of the sensors (*i.e.*, In$_2$O$_3$-P) to 0.125–5 ppm of trimethylamine (TMA) at 350 °C (Fig. 6a–d). For comparison, an In$_2$O$_3$ thin film gas sensor (In$_2$O$_3$-F) with a thickness of 200 nm was fabricated *via* e-beam evaporation (Fig. S5a†). In n-type oxide semiconductors such as In$_2$O$_3$ and SnO$_2$, ionized oxygen adsorption establishes the resistive electron depletion layer near the surface and the reaction between reducing gas and ionized oxygen releases the electrons, which decreases the sensor resistance. That is, the R_a/R_g (R_a: sensor resistance in air, R_g: sensor resistance in gas) value increases upon exposure to reducing gas. The In$_2$O$_3$-P sensor exhibited significantly higher gas response ($S = R_aR_g^{-1}$ at steady state) than the In$_2$O$_3$-F sensor over the entire concentration range of TMA (Fig. 6d). In particular, the gas response of the In$_2$O$_3$-P sensor to 5 ppm TMA (S_T = 239) was ~10 times higher than that of the In$_2$O$_3$-F sensor
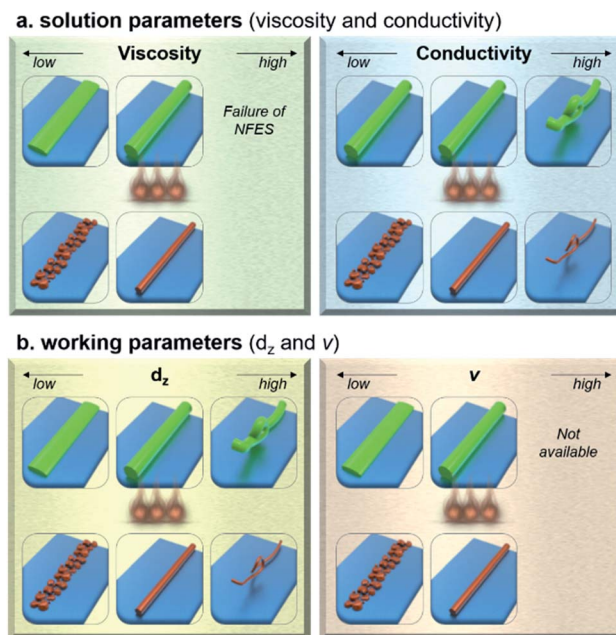

Fig. 5 (a and b) Schematics of the precursor and metal oxide structures with respect to the (a) solution parameters and (b) working parameters.

(S_T = 24). All the nanofibers in the In$_2$O$_3$-P sensor were directly exposed to the ambient atmosphere. In contrast, in the dense In$_2$O$_3$-F sensor, the diffusion of analyte gas into the lower part of sensing film close to the electrodes is difficult and/or a part of analyte gas can be oxidized at the upper part of sensing film, both of which may lead to low gas response. Moreover, polycrystalline nanofibers consisting of numerous chemiresistive grain boundaries are advantageous to achieve a high gas response compared with single crystalline nanowires with a similar diameter.[33] Accordingly, the ultrahigh TMA response of the In$_2$O$_3$-P sensor can be explained by its highly gas-accessible structure and the polycrystalline nature of the nanofibers. The 90% response and recovery times, the times to change 90% of $R_aR_g^{-1}$ variation upon exposure to 5 ppm TMA and air, were 60 s and 108 s, respectively. The In$_2$O$_3$-P sensor exhibited stable and reproducible sensing characteristics under repetitive exposure to TMA, confirming its excellent reliability.

Interestingly, the response of the In$_2$O$_3$-P sensor to 5 ppm of TMA at 350 °C was significantly higher than those to the same concentration of other analytic gases such as ethanol, ammonia, *p*-xylene, toluene, ethylene, and CO (Fig. 6e). The TMA selectivity over ethanol ($S_TS_E^{-1}$) for the In$_2$O$_3$-P sensor was >7, whereas the In$_2$O$_3$-F sensor exhibited similar responses to TMA and ethanol (Fig. 6f). The TMA selectivity (>7) was unusually high considering that the gas responses of most In$_2$O$_3$ gas sensors to TMA and ethanol are reported to be similar (Table S3†).[34–38] Two major differences between the In$_2$O$_3$-P and In$_2$O$_3$-F sensors were the morphology of the sensing materials and the exposure of the sensing electrodes (Pt) to the ambient atmosphere. To examine the effect of electrode exposure on the gas sensing characteristics, randomly oriented In$_2$O$_3$ nanofibers
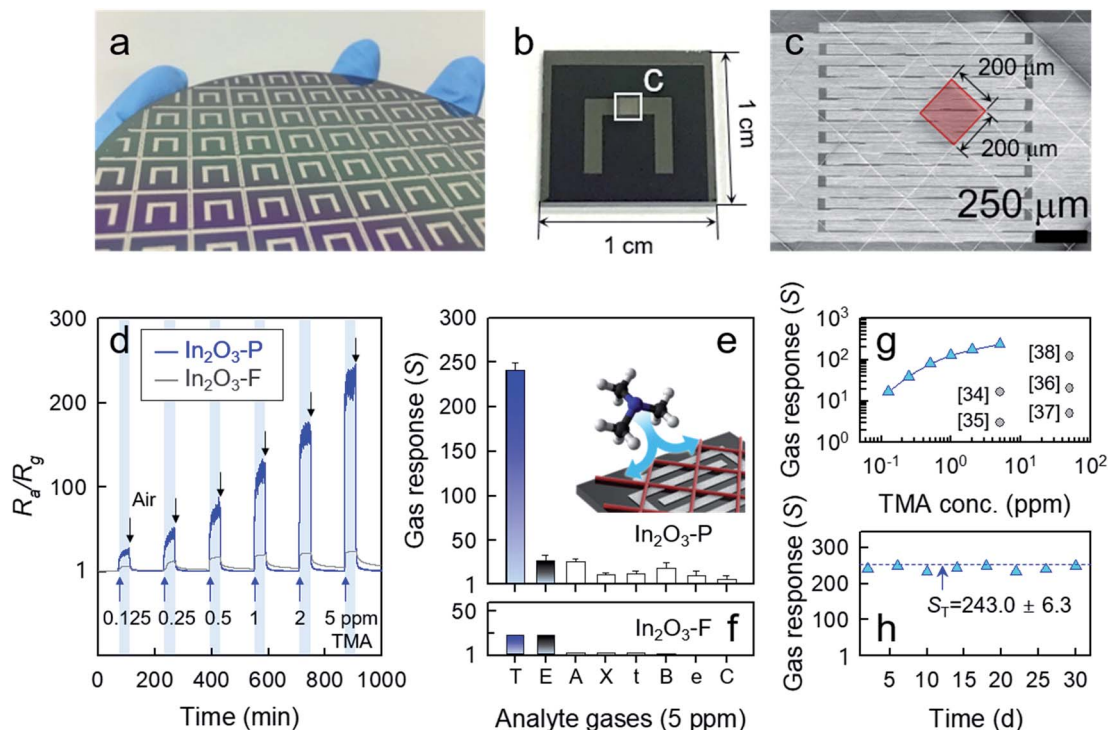
Fig. 6 Optical images of (a) 4-inch SiO_2/Si wafer consisting of 76 sensor substrates and (b) a sensor substrate with Pt interdigitated electrodes. (c) SEM image of In_2O_3-P sensor. (d) Changes in the gas responses of In_2O_3-P and In_2O_3-F sensors upon exposure to 0.125–5 ppm of TMA at 350 °C. Gas responses of (e) In_2O_3-P and (f) In_2O_3-F sensors to 5 ppm of TMA (T), ethanol (E), ammonia (A), p-xylene (X), toluene (t), benzene (B), ethylene (e), and CO (C) at 350 °C (number of measurement in (e): 3). (g) TMA responses of the In_2O_3-P sensor with respect to the TMA concentration. (h) Long-term stability of the In_2O_3-P sensor over 1 month.

with similar diameters and a polycrystalline nature were prepared *via* c-ES and completely coated onto electrodes (Fig. S6a and b†). The random networks of In_2O_3 nanofibers with negligible electrode exposure exhibited lower gas responses and TMA selectivity than the In_2O_3-P sensor (Fig. S6c†). The low gas responses can be explained by the decrease in the gas accessibility, whereas the low selectivity is attributed to the role of the exposed Pt electrodes. Pt is a powerful oxidation catalyst to ethanol.[39] Thus, in the In_2O_3-P sensor, ethanol was readily oxidized into non-reactive or less reactive species at elevated sensing temperature, such as CO_2 or H_2O, by the catalytic Pt with a large area before the gas sensing reaction. In contrast, TMA could be transported toward the sensing materials without significant oxidation.

Most n-type oxide semiconductor chemiresistors generally exhibit relatively low responses to stable and thus less-reactive aromatic gases such as benzene, xylene, and toluene. In contrast, p-type oxide semiconductors such as pure and doped Co_3O_4 or NiO with high catalytic activity often show high responses and selectivity to aromatic gases such as xylene and toluene[40–43] probably because of their abundant oxygen adsorption, multi-valency and facile redox reaction.[44] Accordingly, in order to confirm the general validity of TMA selectivity enhancement assisted by catalytic electrode exposure, we prepared nanofiber pattern sensors with other metal oxides, such as Co_3O_4 (Co_3O_4-P) and NiO (NiO-P), *via* NFES (Fig. S7†) and compared their gas sensing characteristics with those of

thin film counterparts (Fig. S5b, c and S8†). The Co_3O_4-P and NiO-P sensors exhibited not only high selectivity but also high responses to TMA (Fig. S8a and c†), whereas the thin film sensors exhibited comparable responses for all the gases (Fig. S8b and d†). Note that the gas response was defined as '$R_gR_a^{-1}$' in p-type oxide semiconductors because the chemiresistive variation is opposite to n-type semiconductors. Considering above results on In_2O_3, Co_3O_4, and NiO sensors, it is feasible that the interaction between analyte gases with the exposed catalytic electrodes can alter the gas sensing characteristics.[45,46] This clearly indicates that the patterning of metal oxide nanofibers with control of the exposed portion of catalytic electrodes is a general and promising strategy to design highly selective gas sensors and can introduce various new applications of gas sensors.

The TMA responses of the In_2O_3-P sensor in this study were compared with those of In_2O_3 nanostructure gas sensors reported in the literature (Fig. 6g). The results indicated that the responses of the In_2O_3-P sensor were among the highest. The detection limit of TMA was calculated to be ~2 ppb when $S > 1.2$ was used as the criterion for gas detection. TMA, a colorless, flammable, and poisonous gas, is emitted from rotten fish and marine products. Fish is considered as decayed when the TMA concentration is >10 ppm.[47] In addition, TMA causes diseases, including headaches, nausea, skin burns, and eye irritation, when its concentration is >10 ppm.[48] Moreover, sub-ppm levels of TMA are detected in the exhaled breath of patients with

chronic kidney dysfunction and fatty liver disease.[49] Thus, the ultraselective and ultrasensitive In_2O_3-P sensor developed in the present study can be widely used to detect TMA for food monitoring, hazard alarming, and disease diagnosis *via* breath analysis.[48,50] The In_2O_3-P sensor exhibited good stability over 30 days, indicating its potential for practical applications (Fig. 6h). We also demonstrated that NFES is compatible with various substrates (Fig. S9†), suggesting the promising potential of NFES to design functional nanodevices for various applications.

Conclusions

In summary, the on-demand, direct-write fabrication of metal oxide patterns of one-dimensional (1D) nanofibers *via* near-field electrospinning (NFES) was demonstrated, and a comprehensive study was performed on the formation mechanism of the precursor and metal oxide fibers. The key parameters for fiber formation were the volatility, viscosity, and conductivity of the NFES solutions, as well as the needle-to-collector distance and the moving velocity of the nozzle and collector. All the parameters had an optimum window, indicating that the sophisticated control or tuning of the parameters is essential to prepare well-organized and continuous precursor and/or metal oxide fibers *via* NFES. It is worthwhile to note that the longstanding problem of preparing elaborate nano-architectures consisting of 1D metal oxides has been solved for the first time by investigating the interrelations of the solution/working parameters in NFES systematically. Moreover, the patterns exhibited promising potential as functional devices, *e.g.*, gas sensors, as they showed superior selectivity and responses to trimethylamine compared with other metal oxide nanostructures reported in the literature. The results suggest that NFES-fabricated metal oxide nano-architectures are excellent platform materials for new applications of gas sensors. The patterning of metal oxide nanofibers allows precise control over the connectivity of 1D nanofibers, the contacts between nanofibers and electrodes, and the hetero-interfaces between different 1D nanofibers, which will provide new opportunities to develop various next-generation nanodevices such as field effect transistors, light emitting diodes, solar cells, and gas sensors.

Conflicts of interest

There are no conflicts to declare.

Acknowledgements

Notes and references

1 D. H. Sun, C. Chang, S. Li and L. W. Lin, *Nano Lett.*, 2006, **6**, 839–842.

2 A. Hrabec, J. Sampaio, M. Belmeguenai, I. Gross, R. Weil, S. M. Cherif, A. Stashkevich, V. Jacques, A. Thiaville and S. Rohart, *Nat. Commun.*, 2017, **8**, 15765.

3 K. H. Wu, H. H. Cheng, A. A. Mohammad, I. Blakey, K. Jack, I. R. Gentle and D. W. Wang, *Carbon*, 2015, **95**, 738–745.

4 R. Ruiz, H. M. Kang, F. A. Detcheverry, E. Dobisz, D. S. Kercher, T. R. Albrecht, J. J. de Pablo and P. F. Nealey, *Science*, 2008, **321**, 936–939.

5 M. D. Graham, I. G. Kevrekidis, K. Asakura, J. Lauterbach, K. Krischer, H. H. Rotermund and G. Ertl, *Science*, 1994, **264**, 80–82.

6 H. Yoon, H. E. Jeong, T. I. Kim, T. J. Kang, D. Tahk, K. Char and K. Y. Suh, *Nano Today*, 2009, **4**, 385–392.

7 S. S. Williams, M. J. Hampton, V. Gowrishankar, I. K. Ding, J. L. Templeton, E. T. Samulski, J. M. DeSimone and M. D. McGehee, *Chem. Mater.*, 2008, **20**, 5229–5234.

8 R. Ganesan, J. Dumond, M. S. M. Saifullah, S. H. Lim, H. Hussain and H. Y. Low, *ACS Nano*, 2012, **6**, 1494–1502.

9 D. Li, Y. L. Wang and Y. N. Xia, *Adv. Mater.*, 2004, **16**, 361–366.

10 H. Wu, L. B. Hu, M. W. Rowell, D. S. Kong, J. J. Cha, J. R. McDonough, J. Zhu, Y. A. Yang, M. D. McGehee and Y. Cui, *Nano Lett.*, 2010, **10**, 4242–4248.

11 J. Shin, S. J. Choi, I. Lee, D. Y. Youn, C. O. Park, J. H. Lee, H. L. Tuller and I. D. Kim, *Adv. Funct. Mater.*, 2013, **23**, 2357–2367.

12 S. J. Kim, S. J. Choi, J. S. Jang, N. H. Kim, M. Hakim, H. L. Tuller and I. D. Kim, *ACS Nano*, 2016, **10**, 5891–5899.

13 C. Kim, J. W. Jung, K. R. Yoon, D. Y. Youn, S. Park and I. D. Kim, *ACS Nano*, 2016, **10**, 11317–11326.

14 G. S. Bisht, G. Canton, A. Mirsepassi, L. Kuinsky, S. Oh, D. Dunn-Rankin and M. J. Madou, *Nano Lett.*, 2011, **11**, 1831–1837.

15 C. D. Saquing, J. L. Manasco and S. A. Khan, *Small*, 2009, **5**, 944–951.

16 F. Ruggieri, D. Di Camillo, L. Lozzi, S. Santucci, A. De Marcellis, G. Ferri, L. Giancaterini and C. Cantalini, *Sens. Actuators, B*, 2013, **179**, 107–113.

17 Y. Lee, T. S. Kim, S. Y. Min, W. Xu, S. H. Jeong, H. K. Seo and T. W. Lee, *Adv. Mater.*, 2014, **26**, 8010–8016.

18 M. Bognitzki, W. Czado, T. Frese, A. Schaper, M. Hellwig, M. Steinhart, A. Greiner and J. H. Wendorff, *Adv. Mater.*, 2001, **13**, 70–72.

19 C. M. Hsu and S. Shivkumar, *J. Mater. Sci.*, 2004, **39**, 3003–3013.

20 C. W. Kim, D. S. Kim, S. Y. Kang, M. Marquez and Y. L. Joo, *Polymer*, 2006, **47**, 5097–5107.

21 J. J. Schneider, R. C. Hoffmann, J. Engstler, S. Dilfer, A. Klyszcz, E. Erdem, P. Jakes and R. A. Eichel, *J. Mater. Chem.*, 2009, **19**, 1449–1457.

22 C. Tekmen, A. Suslu and U. Cocen, *Mater. Lett.*, 2008, **62**, 4470–4472.

23 S. J. Lee, N. I. Cho and D. Y. Lee, *J. Eur. Ceram. Soc.*, 2007, **27**, 3651–3654.

24 C. Wang, Y. B. Tong, Z. Y. Sun, Y. Xin, E. Y. Yan and Z. H. Huang, *Mater. Lett.*, 2007, **61**, 5125–5128.

This journal is © The Royal Society of Chemistry 2019

J. Mater. Chem. A, 2019, **7**, 24919–24928 | **24927**

25 F. R. Lamastra, F. Nanni, L. Camilli, R. Matassa, M. Carbone and G. Gusmano, *Chem. Eng. J.*, 2010, **162**, 430–435.

26 S. Trocino, P. Frontera, A. Donato, C. Busacca, L. A. Scarpino, P. Antonucci and G. Neri, *Mater. Chem. Phys.*, 2014, **147**, 35–41.

27 I. Moreno, N. Navascues, S. Irusta and J. Santamaria, *J. Catal.*, 2015, **329**, 479–489.

28 M. G. McKee, J. M. Layman, M. P. Cashion and T. E. Long, *Science*, 2006, **311**, 353–355.

29 J. C. Sy, A. S. Klemm and V. P. Shastri, *Adv. Mater.*, 2009, **21**, 1814–1819.

30 J. L. Shui and J. C. M. Li, *Nano Lett.*, 2009, **9**, 1307–1314.

31 G. F. Zheng, W. W. Li, X. Wang, D. Z. Wu, D. H. Sun and L. W. Lin, *J. Phys. D: Appl. Phys.*, 2010, **43**, 415501–415506.

32 C. J. Angammana and S. H. Jayaram, *IEEE Trans. Ind. Appl.*, 2011, **47**, 1109–1117.

33 N. Singh, A. Ponzoni, R. K. Gupta, P. S. Lee and E. Comini, *Sens. Actuators, B*, 2011, **160**, 1346–1351.

34 C. S. Lee, I. D. Kim and J. H. Lee, *Sens. Actuators, B*, 2013, **181**, 463–470.

35 P. Rai, J. W. Yoon, C. H. Kwak and J. H. Lee, *J. Mater. Chem. A*, 2016, **4**, 264–269.

36 X. F. Lu, Q. Q. Yu, K. Wang, L. C. Shi, X. Liu, A. G. Qiu, L. Wang and D. L. Cui, *Cryst. Res. Technol.*, 2010, **45**, 557–561.

37 X. Sun, X. J. Liu, X. L. Deng and X. J. Xu, *RSC Adv.*, 2016, **6**, 89847–89854.

38 S. X. Shi, F. Zhang, H. M. Lin, Q. Wang, E. B. Shi and F. Y. Qu, *Sens. Actuators, B*, 2018, **262**, 739–749.

39 T. Mallat and A. Baiker, *Chem. Rev.*, 2004, **104**, 3037–3058.

40 Y. M. Jo, T. H. Kim, C. S. Lee, K. Lim, C. W. Na, F. Abdel-Hady, A. A. Wazzan and J. H. Lee, *ACS Appl. Mater. Interfaces*, 2018, **10**, 8860–8868.

41 J. W. Yoon, Y. J. Hong, G. D. Park, S. J. Hwang, F. Abdel-Hady, A. A. Wazzan, Y. C. Kang and J. H. Lee, *ACS Appl. Mater. Interfaces*, 2015, **7**, 7717–7723.

42 B. Y. Kim, J. W. Yoon, J. K. Kim, Y. C. Kang and J. H. Lee, *ACS Appl. Mater. Interfaces*, 2018, **10**, 16605–16612.

43 H. J. Kim, J. W. Yoon, K. I. Choi, H. W. Jang, A. Umar and J. H. Lee, *Nanoscale*, 2013, **5**, 7066–7073.

44 H. J. Kim and J. H. Lee, *Sens. Actuators, B*, 2014, **192**, 607–627.

45 N. Barsan, D. Koziej and U. Weimar, *Sens. Actuators, B*, 2007, **121**, 18–35.

46 A. Ylinampa, L. Lantto and Leppävouri, *Sens. Actuators, B*, 1993, **13–14**, 602–604; *Sens. Actuators, B*, 2018, **262**, 739–749.

47 K. Mitsubayashi, Y. Kubotera, K. Yano, Y. Hashimoto, T. Kon, S. Nakakura, Y. Nishi and H. Endo, *Sens. Actuators, B*, 2004, **103**, 463–467.

48 https://www.cdc.gov/niosh/pel88/75-50.html, accessed 02 September 2019.

49 N. Alkhouri, F. Cikach, K. Eng, J. Moses, N. Patel, C. Yan, I. Hanouneh, D. Grove, R. Lopez and R. Dweik, *Eur. J. Gastroenterol. Hepatol.*, 2014, **26**, 82–87.

50 C. H. Kwak, H. S. Woo and J. H. Lee, *Sens. Actuators, B*, 2014, **204**, 231–238.